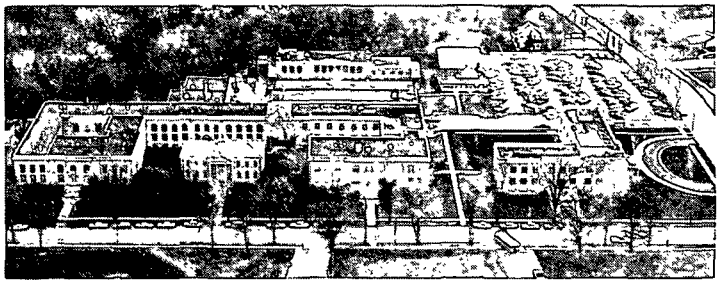

THE INSTITUTE OF PAPER CHEMISTRY, APPLETON, WISCONSIN

IPC TECHNICAL PAPER SERIES

NUMBER 118

ULTRASONIC CHARACTERIZATION OF FIBER SUSPENSIONS

C. C. HABEGER AND G. A. BAUM

NOVEMBER, 1981

ULTRASONIC CHARACTERIZATION OF FIBER SUSPENSIONS

C. C. Habeger and G. A. Baum
The Institute of Paper Chemistry

ABSTRACT

This paper presents the results of an experimental and theoretical investigation into the fundamental mechanisms that govern ultrasound propagation in fiber slurries. An experimental apparatus which measures the attenuation and velocity of ultrasound in slurries is described. Measurements on wood fiber slurries show that the effect of the fiber on the velocity of ultrasound is negligible in contrast to previous work. This observation led to the development of an isolated segment model, which can predict attenuation as a function of fiber properties and frequency. The theory assumes the fibers are isolated, isotropic, infinite cylinders. It accounts for scattering, heat conduction, viscous losses in the fluid, and relaxation processes in the fiber. Experiment and theory are shown to be in good agreement for some synthetic fiber slurries. In the more complicated case of wood fiber suspensions, the theory predicts attenuation to the correct order of magnitude and permits speculation about the effects of fiber properties.

INTRODUCTION

A nondestructive analysis of fiber slurries using ultrasonic techniques may someday be a valuable tool for determining fiber properties. Previous authors (1-2) have shown that the attenuation of ultrasound in wood fiber suspensions is proportional to consistency. They have also demonstrated that the attenuation at a given consistency varies with furnish. Adams (2) reported that the attenuation is also a function of the amount of refining. Ultrasonic attenuation is thus sensitive to the origin and treatment of a wood fiber suspension. It should be possible to characterize the slurry by measuring attenuation as a function of frequency. However, progress in this area is hampered by the lack of understanding of wave propagation in fiber suspensions. In fact, from previous work, it is not even possible to identify the major loss processes.

The theoretical models of wave propagation in heterogeneous fluid-solid mixtures can be classified as isolated segment models or as porous solid models. The isolated segment models calculate the loss due to a single solid element surrounded by the fluid and assume that the total loss is the sum of the effects of the individual elements. Interactions between solid elements are not considered. An example of this, for cylindrical segments, is the Rayleigh-Sewell model (3). Here, losses from scattering and viscous processes caused by rigid, immovable cylindrical inclusions in a viscous fluid are calculated. The Rayleigh-Sewell model predicts that the slope of $\ln(\alpha/f^2)$ vs. $\ln(f)$ should always increase with f (α is the attenuation coefficient and f is frequency). This is contrary to the experiments on wood fiber suspensions of McFarlane and Llewellyn (1) and Adams (2). A more complete isolated segment model is that of Allegra and Hawley (4). It allows for shear and normal strains in the solid, considers thermodynamic effects, and accounts for relaxation processes in the solid. The Allegra-Hawley theory can predict the attenuation vs. frequency behavior of polystyrene spheres in water from independently determined bulk properties of water and polystyrene (4). Curiously, in the range of frequencies and radii studied, energy dissipation due to heat conduction in the solid-fluid boundary region is the dominant loss

process. Unfortunately, the Allegra-Hawley model is developed only for spherical segments and is not applicable to fiber suspensions.

In the porous solid models, the solid fraction is assumed to form a porous structure, and the mechanical properties of the structure are important. The Biot model (5) is a well-developed porous solid theory which assumes that the fluid is contained in parallel cylindrical capillaries and that attenuation arises from viscous flow in the capillaries. It is possible to include solid relaxation processes, but scattering and thermal loss processes are ignored. An additional drawback of the Biot theory is the difficulty of estimating model parameters. It is hard to obtain the bulk fiber properties needed by the isolated solid theories, but the mechanical parameters for the structures and the interaction parameters between structure and fluid, needed by the Biot model, are far more difficult.

If frequency-dependent velocity changes existed and could be measured along with attenuation, additional information for slurry characterization would be available. This is the path taken by Adams (2), who made velocity and attenuation measurements. Adams reported that wood fibers do cause a frequency-dependent velocity shift. Since porous solid models predict a frequency-dependent velocity shift, while isolated segment models do not, Adams selected the Biot model to explain his results. Adams also obtained data indicating that attenuation is not linear when different fractions of two different pulps are mixed. This is counter to the predictions of the isolated segment models. In contrast, McFarlane and Llewellyn (1) and Adams (2) found that attenuation is linear with solid fraction, an observation more in line with the isolated segment models than the porous solid models. Adams did not attempt to predict his experimental results from independent determinations of the Biot parameters, but he did show that Biot parameters do exist which give the observed shape of the velocity and attenuation curves.

EXPERIMENTAL

The apparatus we constructed to measure ultrasound velocity and attenuation in fiber slurries is a pulsed radio frequency (rf) interferometer designed to operate from 0.6 MHz to 13 MHz. Adams used a similar design.

A schematic is shown in Figure 1. The rf signal from a stable continuous wave (CW) source is mixed with a pulse to produce a pulsed rf signal. This is applied to a piezoelectric transmitter which is immersed in the suspension. An identical transducer receives the signal after it has passed through a length, L, of fiber suspension. The signal received is attenuated to a standard level, amplified, and mixed with the continuous wave.

- FIGURE 1 HERE -

The phase of the received signal depends on the phase shift in the suspension, $2\pi Lf/V$, and the phase shift in the transducers. Here f represents the frequency of the CW signal, and V is the velocity of sound in the suspension. The amplitude of the mixed signal is a maximum when the phase difference between the CW signal and the received signal is an integral multiple of 2π. As frequency changes, the phase of the received signal progresses and the mixed output oscillates. The velocity of sound in the suspension can be calculated from the frequency difference between minima in the mixed output, provided the phase shifts outside the suspension can be accounted for. The attenuation in the suspension can be determined from the value of attenuation necessary to produce the standard signal level.

In order to obtain very accurate velocity measurements, our apparatus differed from Adams' in two ways. The CW signal source is not an oscillator, but a frequency synthesizer stable to one part in 10^7. This gives a resolution of one part in 10^5 in the frequency shift measurements on homogeneous fluids. In addition, the transducers are mounted so that their separation distance can be varied. This allows the frequency-dependent phase shifts in the transducers to be measured, thus allowing correction of the velocity data. Adams estimated these shifts from a mathematical model of the transducers.

The suspension is contained in a plexiglass chamber 50 cm long by 20 cm wide by 20 cm high (see Figure 2). Four transducer pairs are mounted in a frame and suspended above the slurry on precision screws. This allows the transducer separations to be varied. The four transducer pairs are necessary to cover the frequency range from 0.6 MHz to 13 MHz. The entire assembly is immersed in a water bath whose temperature is controlled to within 0.01°C. The suspension is mixed by a pair of stirrers mounted behind the transducer assemblies and rotating in opposite directions.

-FIGURE 2 HERE -

A second technique can be used for measuring the ultrasound velocity. The sample chamber can be separated into two parts by inserting a 0.006-mm-thick Mylar membrane between the transducer assemblies. By placing water in one compartment and the fiber suspension in the other, the velocity can be measured by a second technique. The transducer assemblies are moved along the supporting screws with their separation fixed, thus changing the relative amounts of water and fiber seen by the transducer pairs. The velocity is then calculated from the change in distance necessary to move the mixed output signal between minima.

VELOCITY MEASUREMENTS

Equation (1) gives the velocity of sound, V, in the fluid, accounting for the frequency-dependent phase shifts in the transducers.

$$V = \frac{L\Delta f}{1 - \frac{d\phi}{df}\frac{\Delta f}{2\pi}} \tag{1}$$

Here L is the transducer separation, Δf is the frequency difference between minima in the mixed signal output, and $\frac{d\phi}{df}$ is the derivative of the total transducer phase shift with respect to frequency. By making measurements at two transducer separations and setting the resulting left hand side of Equation (1) equal, the transducer effect can be calculated.

The transducer effect in terms of the Δf's at two separations is

$$w = \frac{1}{2\pi}\frac{d\phi}{df} = \frac{(L_2\Delta f_2 - L_1\Delta f_1)}{\Delta f_1 \Delta f_2 (L_2 - L_1)} \tag{2}$$

This approach was first tested on distilled water. Measurements of Δf were made with the four transducer pairs at three separation distances (5, 10, and 15 cm). The three possible values of w were calculated and averaged. The velocity was then calculated from Equation (1) for the three values of L and Δf. The results for one transducer pair (5 MHz) are shown in Figure 3. The three lower solid curves represent the apparent velocities ($L\Delta f$) at each separation distance,

and the top solid curve is the average corrected curve for distilled water. The corrected water values for all frequencies were within 0.15% of the table value of the velocity in distilled water. At frequencies above 1.2 MHz, the agreement was better than 0.07%. The system thus provides a stable and accurate measurement of the velocity of ultrasound in homogeneous fluids.

- FIGURE 3 HERE -

The results of the same procedure for a 0.48% consistency, 90 C.S.F., bleached kraft pulp are shown in Figure 3 as dashed lines. The pulp slurry has a different mechanical impedance than water only, and the correction for transducer phase shifts is smaller. Over the entire 0.6 - 13 MHz range, the corrected velocity of the pulp is an average of 0.06% higher than that of water, with a standard deviation of 0.05%. So, there is a small increase in velocity, but no significant frequency dependence.

Tests were conducted on pulps up to approximately 3% consistency. The apparent velocity was measured only at the 5-cm separation, and the w's calculated from the water experiments were used to calculate the corrected velocities. This tends to overestimate the slurry velocity. However, the largest deviation from the distilled water value was only +0.6%, and again no frequency dependence was detected.

Since the effect of fibers on the velocity of ultrasound in water is a crucial question, the second velocity measurement technique was also used. This was the water-diaphragm-pulp method discussed above. A constant 15-cm separation was maintained between transducers, and the apparent velocity was measured as the transducers were moved relative to diaphragm. As the transducers move, the errors due to transducer phase shifts remain constant. The only change, therefore, was in the path lengths of the ultrasound in pulp and water. These measurements were made with a 0.96% consistency, 90 C.S.F., bleached kraft pulp and a 0.77% consistency, 720 C.S.F., bleached kraft pulp. For the 720 C.S.F. pulp the velocity was 0.12% ($\pm$0.11%) greater than water, and for the 90 C.S.F. pulp the velocity was 0.12% ($\pm$0.4%) greater than water. This is consistent with our earlier results.

We must conclude that the velocity of ultrasound in a wood fiber suspension does not, to first order, differ from the velocity in water and is not frequency dependent. The above results allow us to reject the porous solid models discussed earlier and to use an isolated segment model to explain the attenuation results. Such models have parameters that are more likely to be independently determined. The Allegra-Hawley model is the only isolated segment model complete enough to realistically handle polymeric fiber suspensions, but it only applies to spherical inclusions. It was necessary, therefore, to develop an Allegra-Hawley model for infinite length cylindrical inclusions. The resulting theory, which will be published elsewhere, is outlined in the Appendix and briefly described below.

THEORY

The Allegra-Hawley model for spheres calculates the attenuation by finding an exact solution for the strain and temperature to the governing differential equations of continuity, motion, and energy conservation. The model considers a single solid segment in a fluid medium. The solution must be a plane compressional wave far away from the inclusion, and the boundary conditions of equal stress, velocity, temperature, and heat flux must be met over the solid-fluid interface. The solution is found by expanding the incoming plane wave in terms of

spherical harmonics. Solutions are expressed in terms of three scalar potentials in the fluid and three in the solid. The total solution is the plane wave plus the potentials expanded in spherical harmonics with undetermined coefficients. The coefficients are found by applying the boundary conditions to each order of spherical harmonics. The result is six equations and six unknowns for each order. These are solved numerically for the zeroth, first, and second order. As long as the radius of the sphere is less than the wavelength of the compressional wave, the series converges rapidly, and the first few orders are sufficient. The attenuation is calculated from these coefficients.

In order to apply this model to fibers, the calculation is repeated for infinite cylindrical, isotropic inclusions. For this case the plane waves and potential functions are expanded in terms of Bessel functions and sinusoidal functions. For the spherical case, symmetry arguments show there is no velocity or stress in the ϕ direction. For the cylinder there are velocities and stresses in the z, r, and θ directions; therefore, there are more boundary conditions and a fourth potential is needed. In addition, the solution depends on the orientation of the incoming wave to the plane of the cylinder; thus, attenuations are found for a set of orientations and numerically integrated to get the result for randomly orientated fibers. The result of this theoretical development is a computer program that gives the attenuation as a function of frequency when the following parameters are given: cylinder radius (R'); solid and fluid compressional wave velocity (c',c); densities (ρ',ρ); solid Poisson's ratio (ν'); fluid viscosity (η); the thermal conductivities (K', K); the thermal expansion coefficients (β',β); the heat capacities (Cp',Cp); temperature (T); solid loss tangent ($\tan\delta$); and solid volume fraction (fr).

Although the different processes interact, it is possible to make some qualitative statement about the relative importance of scattering, viscous losses, thermal losses, and solid relaxation processes. Thermal effects peak at a frequency where the skin depth of the thermal wave is of the order of the radius. For the radii of interest (1 to 100 μm) this happens below the lowest experimental frequency (0.6 MHz), and thermal processes make a significant contribution only for the thinnest fibers at the lowest frequencies. Since in most cases this means that the thermodynamic coefficients are not important, the complexity of the prediction process is reduced. Viscous drag is a maximum when the skin depth of the fluid viscous wave is of the order of the radius. This is at a higher frequency than for the thermal case. Viscous processes make a strong contribution at the lower frequencies and radii studied. Relaxation always contributes, and can be dominant when the loss tangent is large and there is a good impedance match between fluid and solid. Scattering is a major factor at the higher radii and frequencies.

Limitations of the theory when applied to actual fiber suspensions result from (1) fiber anisotropy, (2) finite fiber length and (3) noncylindrically shaped fibers. Concerning Item 2, a difference between finite and infinite fibers arises when $\tan\delta$ is small. Figure 4 shows theoretical plots of the relative attenuation of a single fiber as a function of ε, the angle between the plane of the fiber and the incoming radiation, at different values of loss tangent. Notice the strong peak for low loss tangents. This occurs when the wavevector of the incoming radiation, as projected along the fiber, equals the wavevector of the zeroth order longitudinal rod mode in the cylinder. The velocity of this mode is approximately $(E'/\rho')^{1/2}$ when the wavelength of the bulk compressional wave in the solid is much greater than the radius (E' is Young's modulus of solid and ρ' is the solid density). At this angle in the infinite cylinder, disturbances from the incoming radiation on the cylinder interfere constructively, and large motions are excited in the cylinder. This phenomenon requires communication between distant parts of

the fiber and would not be seen experimentally on short fibers. When $\tan\delta$ is high, communication over larger distances is lost, even in infinite cylinders, and the theory is more applicable. Differences between experiment and the infinite cylinder model are expected when the quantity $2\pi f \tan\delta / c'$ is less than the inverse fiber length.

- FIGURE 4 HERE -

ATTENUATION RESULTS

Preliminary attenuation measurements on wood fiber slurries confirmed many of the results reported by Adams (2). Within experimental error, attenuation was proportional to consistency. This was also true for the synthetic fiber systems. Air bubbles had a large effect on attenuation at the lower frequencies. Slurries had larger attenuation before degassing at frequencies below about 2 MHz. Because of the air effect, slurries were routinely degassed overnight before testing. Also, as will be discussed later, refining tended to decrease the attenuation in bleached kraft pulps.

Because of problems in characterizing wood pulp fiber systems, the majority of the data presented here are from synthetic fiber suspensions. Such fibers have similar dimensions and physical properties. This is helpful in identifying those parameters which are most important in ultrasound attenuation. The properties of the synthetic fibers studied are included in Table I.

-TABLE I HERE -

The results of the experimental and theoretical attenuation studies are reported by fiber category. The data are represented, as is customary, by plots of attenuation divided by frequency squared vs. frequency. The attenuation data are divided by the consistency to normalize the curves to a 1% consistency slurry. The data come from four transducers at two separations (10 cm and 15 cm) and often two consistencies.

NYLON

Nylon is very hydroscopic, and water acts as an effective plasticizer. This leads to a relatively high loss tangent. For swollen nylon fibers in the frequency range studied, handbook values indicate a loss tangent value of between 0.1 and 0.2. The theoretical model predicts that thermal phenomena should not have a significant effect on the attenuation. Thermal processes would contribute if the radii were of the order of 1 μm, or if the measuring frequency were two orders of magnitude smaller (10 kHz).

Figure 5 gives results for a slurry made from a 15.2 $\pm$ 1 μm radius nylon 6,6 fiber, cut to lengths of 2.3 mm.

- FIGURE 5 HERE -

The model requires that the elastic properties of the fibers be known. For an isotropic solid two independent elastic parameters must be specified. The longitudinal wave velocity in a rod can be measured to fix one parameter since this velocity equals $(E'/\rho')^{1/2}$. Using techniques developed for in-plane measurements on paper, the velocity of this mode in the saturated nylon fibers was 1.66 mm/μsec at 60 kHz. The Poisson ratio, ν', is taken as the other unknown parameter. One could also use the fiber shear modulus, μ', since $\mu' = E'/2(1 + \nu')$.

In Figure 5, for the theoretical attenuation curve the loss tangent was set equal to 0.1, the lower handbook value. Actually the effect of tanδ on these curves is quite small, a change of tanδ from 0.05 to 0.2 causing only 10% difference in the curves. The only significant unknown parameter, therefore, is the Poisson's ratio, and this may be varied to obtain the best fit. Good agreement between experiment and theory occurs when $\nu' \simeq 0.3$.

The value of $k_c'\rho'$ tanδ is one at about 1.4 MHz, indicating that deviation between theory and experiment might be expected at the lower frequencies, due to the finite length of the fibers.

The effect of radius can be predicted by calculating theoretical curves at the same consistency, but with different radii. The results show that attenuation increases somewhat with radius, e.g., $(\frac{d \ln \alpha}{d \ln R'} \simeq 0.27$ at 1 MHz).

Figure 6 shows the results for a much larger ($R' = 115 \pm 5$ μm) nylon 6 fiber. The theoretical plots show the effects of different loss tangents. The Poisson's ratio is assumed to be 0.3 because of the good fit in Figure 5. Because of difficulties in measuring ultrasound velocities in saturated fibers of this type, the longitudinal velocity was estimated by assuming that the ratio between the wet and dry state is the same in this sample as in the other nylon fibers tested. The maximum in the attenuation at 1.7 MHz for both theoretical experimental curves is due to scattering. Notice that the low tanδ theoretical curve has three scattering peaks. These peaks become more prominent at still lower tanδ's. The loss tangent appears to have a significant effect at the lower frequencies but becomes inconsequential once scattering dominates.

- FIGURE 6 HERE -

POLYESTER

The attenuation data for 2.3-mm-long polyester fibers with 13 μm radii and 4.0 mm/μsec rod velocities are shown in Figure 7. Figure 8 shows the results for the same material cut to 1.6-mm lengths. The evenly spaced oscillations in the experimental data are surprising.

- FIGURE 7 AND 8 HERE -

Unlike nylon, polyester is not hydroscopic and has a small loss tangent. The theoretical curves are insensitive to tanδ, making ν' the only adjustable parameter. It is possible to choose a value of ν' such that the theory predicts the average behavior of experiments. The solid lines in Figures 7 and 8, which approximate the data if the oscillations are ignored, have $\nu' = 0.4$. This average fit may be fortuitous because for the 2.3-mm fibers, $k_c'\ell'$ tanδ is one at about 17 MHz. This means that the infinite cylinder model should not be applicable over most of the frequency range.

The explanation for the observed oscillations becomes clear when it is noticed that the period and phase are length dependent. The loss tangent is small and the fibers are short enough that a significant resonant vibration can occur when the fiber length is an integral number of half wavelengths of the longitudinal rod mode. The frequencies at which the first resonance should occur, using the measured rod velocities, are marked at the top of Figures 7 and 8. This resonance phenomenon, of course, is not predicted by the infinite cylinder theory.

RAYON

Rayon is similar to nylon in that it is hydroscopic, and the water acts as a plasticizer. The velocity of the longitudinal rod wave in saturated rayon is less than nylon; therefore, finite length effects are even less significant than in nylon. For the fiber radii studied ($R' > 7$ μm), thermal effects are only a few percent. Preliminary theoretical curves indicate that attenuation is more sensitive to $\tan\delta$ in rayon than in nylon. This means there are two adjustable parameters, $\tan\delta$ and ν' (fiber modulus is found from the measured rod velocities). Loss tangent is a function of frequency; but, for simplicity, the model curves assume constant $\tan\delta$.

Figure 9 shows the theoretical and experimental curves for a normal modulus, 9.0 μm in radius, 2.3-mm-long rayon fiber. The Poisson ratio is set at 0.32, and $\tan\delta$ is varied to produce different model curves. The rod longitudinal velocity was measured as 0.91 mm/μsec. There is good agreement with experiment when $\nu \simeq 0.32$ and $\tan\delta \simeq 0.1$, but there are surely other combinations giving an equally good fit. Figure 10 is a set of model curves for this rayon fiber with $\tan\delta = 0.1$ and variable Poisson ratios. Notice this trend is the reverse of nylon (Figure 5) where increasing ν' (or decreasing shear modulus) led to increasing attenuation.

- FIGURE 9 AND 10 HERE -

Figure 11 shows the experimental results for a 7.5 μm high wet modulus rayon fiber slurry. The rod longitudinal velocity is 1.27 mm/μsec in the saturated fiber. The level of attenuation is about the same as the other rayon fiber, although the curve is flatter at the lower frequencies. Reasonable values of $\tan\delta$ and ν' can be chosen to give the correct average value of attenuation, but the theory is not as successful in reproducing the shape of the curve. It is possible that the theory is less suitable for high wet modulus rayon because it is more elastically anisotropic. Another possible explanation is that there is a viscoelastic absorption peak in this frequency regime and $\tan\delta$ varies rapidly with frequency. This is consistent with the observation that the $\tan\delta$ necessary to fit average theory to experiment is greater than the $\tan\delta$ in the regular rayon.

- FIGURE 11 HERE -

WOOD FIBERS

Figure 12 shows the experimental data for a bleached kraft softwood pulp at different refining levels. Each data point is the average of about 25 measurements. The data are taken on pulp with consistencies from 0.48% to 2.89%. The transducer separation distance varies from 5 to 15 cm. Important points to notice are the following:

1) the level of attenuation is considerably lower than that measured for rayon fibers;
2) there is a remarkably larger decrease in attenuation during the early stages of refining;
3) for highly beaten pulp the decrease wanes and reverses at the lower frequencies.

- FIGURE 12 HERE -

Wood fiber slurries are, of course, much more complex than synthetic fiber slurries. There are broad distributions in the shapes and sizes of the fibers, and the cross sections are not cylindrical. The mechanical and

thermodynamic properties vary in a similar way and are not easily determined. Beating is not well understood in terms of its effect on the geometric, thermodynamic, and mechanical fiber properties. Nonetheless, using insight gained from the work on synthetic fibers, it is possible to conjecture as to what may be happening in this wood pulp system.

A possible explanation for the difference between rayon and wood fibers in the level of attenuation may be due to a higher degree of crystallinity in the wood fibers. This leads to a lower loss tangent and, therefore, a lower attenuation. It was shown in Figure 9 that rayon is quite sensitive to changes in loss tangent.

There are a number of changes occurring during refining that could alter the curves. The theory predicts that a decrease in the representative radius of the fibers would lower the attenuation. However, this effect is not large enough to explain the large decrease in attenuation brought about by refining, if the radius is assumed to initially be less than about 20 μm. Large particles (50 to 500 μm radii) in the slurry would have a scattering peak in the experimental frequency range. Although small in number, these particles could make a large contribution, and if refining reduced their number, it could significantly reduce attenuation.

One effect of refining could be to reduce the fiber shear modulus while keeping Young's modulus relatively constant. In the theoretical model, this corresponds to an increase in ν' at constant rod longitudinal velocity. As shown in Figures 5 and 10, changing ν' can have a large effect on attenuation. For rayon fibers, where the velocity of the longitudinal wave in the fiber is lower than in water, increasing ν' decreases attenuation. For nylon, where the velocity is greater than in water, the trend reverses. Wood fibers probably have a greater velocity than rayon and may be in a transition region. If the wet modulus of the wood fibers is not too much greater than that in rayon, the decrease in attenuation with refining might be due to decreasing shear modulus with refining.

It is clear that more work needs to be done on well-characterized wood pulp systems before we have a clear understanding of ultrasound attenuation in pulp. However, the major effects have been identified. Quantitative results have been correctly predicted for synthetic fiber systems, and qualitative explanations for the observed behavior in wood pulp systems suggest that further study is warranted.

REFERENCES

1. McFarlane, I. D. and Llewellyn, J. D. Paper 2.2, 2nd International Federation of Automatic Controls, Proc. Brussels, 1971.

2. Adams, D. J. 3rd International Federation of Automatic Control Proc. Brussels, 1976. p. 187.

   Adams, D. J. Ultrasonic Transmission Through Paper Fiber Suspensions. Ph.D. Thesis. University of London, 1975.

3. Lord Rayleigh. Theory of Sound. Vol. II. Dover, 1945.

4. Allegra, J. R. and Hawley, S. A., J. Acoust. Soc. Am. 51(5, Part 2):1545 (1972).

5. Biot, M. A., J. Acoust. Soc. Am. 28(2):168, 179(1956); 33(4):1482(1962).

6. Epstein, P. S. and Carhart, R. R., J. Acoust. Soc. Am. 25(3):553(1953).

APPENDIX

OUTLINE OF THE THEORETICAL DEVELOPMENT

List of Symbols*

r,θ,z	Cylindrical coordinates aligned with the fiber
t	Time
R'	Cylinder radius
T	Temperature
fr	Solid volume fraction
ω	Angular frequency
ϵ	Angle between the plane of the fiber and the incoming radiation
$\vec{A}$	Transverse wave vector potential
ϕ	Compressional wave potential
ψ,ξ	Scalar potentials for transverse wave
c	Velocity of compressional wave
ℓ'	Fiber length
ρ	Density
η	Viscosity
ν'	Solid Poisson's ratio
μ'	Solid shear Lame constant $\frac{(0.5-\nu')\rho' c'^2}{(1-\nu')}[1-i\tan\delta]$
K	Heat conductivity coefficient
C_p	Heat capacity
β	Thermal expansivity
$\tan\delta$	Solid loss tangent
k_c	ω/c
a_c	$R'kc$
k_c'	$w/c'(1-i\tan\delta)^{1/2}$
a_c'	$R'k_c$
k_{cs}	$k_c\sin\epsilon$
a_{cs}	$R'k_{cs}$
k_{cc}	$k_c\cos\epsilon$
a_{cc}	$R'k_{cc}$
k_{cc}'	$[k_c'^2-k_{cs}^2]$
a_{cc}'	$R'k_{cc}'$
k_t	$(i\omega\rho C_p/K)^{1/2}$
a_t	$R'k_t$
k_{tc}	$[k_t^2-k_{cs}^2]^{1/2}$
a_{tc}	$R'k_{tc}$
k_s	$(i\omega\rho/\eta)^{1/2}$
a_s	$R'k_s$
k_s'	$\omega(\rho'/\mu')^{1/2}$
a_s'	$R'k_s'$
k_{sc}	$(k_s^2-k_{cs}^2)^{1/2}$
k_{sc}'	$(k_s'^2-k_{cs}^2)^{1/2}$
a_{sc}	$R'k_{sc}$
b_c	$-\beta T\omega^2/Cp$
C_{12}	$c^2+4i\omega\eta/3\rho$
C_{12}'	$c'^2-4\mu'/3\rho'$
γ	$1+\beta^2 Tc^2/Cp$
b_t	$[(C_{12}/\rho-4i\omega\eta/3\rho)k_t^2-\omega^2]\gamma/C_{12}\alpha$
b_t'	$[(C_{12}'/\rho'+4\mu'/3\rho')k_t'^2-\omega^2]\gamma'/C_{12}'\alpha'$
J_n	n'th Order Bessel function of 1st kind
$H_n^{(1)}$	n'th Order Hankel function of 1st kind
J_n'	1st Derivative of J_n
J_n''	2nd Derivative of J_n
$H_n^{(1)}'$	1st Derivative of $H_n^{(1)}$
$H_n^{(1)}''$	2nd Derivative of $H_n^{(1)}$
B_n,C_n,D_n,E_n	Undetermined coefficients
s	Consistency
f	Frequency
$\vec{V}$	Velocity vector

*Prime symbols refer to the solid. Unprimed symbols refer to the fluid. When primed coefficients are unlisted they have definitions analogous to the unprinted symbols.

The problem is to find a solution for temperature and velocity to the continuity equation, the equations of motions, and the energy conservation equation which meets the required boundary conditions at the cylinder-fluid interface and is a plane wave at an angle ε to the plane of the cylinder far from the cylinder. It is shown by Epstein and Carhart (6) and Allegra and Hawley (4) that the governing equations can be linearized for small motions and expressed in terms of potentials, A's and ϕ's. The governing equations are satisfied if equations (1)-(4) are obeyed and the velocity and temperature are related to the potentials as in Equations (5) and (6).

$$\vec{\nabla}\cdot\vec{A} = 0 \tag{1}$$

$$\nabla^2\phi_c = -k_c{}^2\phi_c \tag{2}$$

$$\nabla^2\phi_t = -k_t{}^2\phi_t \tag{3}$$

$$\vec{\nabla}x\vec{\nabla}x\vec{A} = -k_s{}^2\vec{A} \tag{4}$$

$$\vec{V} = -\vec{\nabla}\phi_c - \vec{\nabla}\phi_t + \vec{\nabla}x\vec{A} \tag{5}$$

$$T = b_c\phi_c + b_t\phi_t \tag{6}$$

Equations similar to (1)-(6) apply in the solid. Here the corresponding symbols will be denoted by a prime.

When the incoming plane wave is expanded in terms of Bessel functions, it becomes

$$\phi_o = [J_o(k_{cc}r) + 2\sum_{n=1}^{\infty} i^n\cos n\theta\ J_n(k_{cc}r)]e^{i(k_{cs}z-\omega t)} \tag{7}$$

Solutions to Equations (2) and (3) can be expanded similarly with undetermined coefficients. The results are:

$$\phi = \phi_o + \phi_r + \phi_t, \text{ and} \tag{8}$$

$$\phi' = \phi_c' + \phi_t' \tag{9}$$

Where

$$\phi_r = [B_oH_o^{(1)}(k_{cc}r) + 2\sum_{n=1}^{\infty} B_ni^n\cos n\theta\ H_n^{(1)}(k_{cc}r)]e^{i(k_{cs}z-\omega t)}, \tag{10}$$

$$\phi_t = [C_oH_o^{(1)}(k_{tc}r) + 2\sum_{n=1}^{\infty} C_ni^n\cos n\theta\ H_n^{(1)}(k_{tc}r)]e^{i(k_{cs}z-\omega t)}, \tag{11}$$

$$\phi_c' = [B_o'J_o(k_{cc}'r) + 2\sum_{n=1}^{\infty} B_n'i^n\cos n\theta\ J_n(k_{cc}'r)]e^{i(k_{cs}z-\omega t)}, \text{ and} \tag{12}$$

$$\phi_t' = [C_o'J_o(k_{tc}'r) + 2\sum_{n=1}^{\infty} C_n'i^n\cos n\theta\ J_n(k_{tc}'r)]e^{i(k_{cs}z-\omega t)}. \tag{13}$$

In the above, solutions which have the same time and z dependence as the incoming radiation [i.e., $e^{i(k_{cs}-\omega t)}$] are being sought.

The boundary conditions at r = R' are (a) $V_r = V_r'$; (b) $V_\theta = V_\theta'$; (c) $V_z = V_z'$; (d) $T = T'$; (e) $KT,r = K'T',r$; (f) $t_{rr} = t_{rr}'$; (g) $t_{r\theta} = t_{r\theta}'$; and (h) $t_{rz} =$

t_{rz}'. To meet these eight boundary conditions, two linearly independent solutions to equations (1) and (4) are needed. It can be shown that A_1 and A_2 are solutions to equations (1) and (4) when $A_1 = \vec{\nabla} \times \Psi\hat{k}$ and $A_2 = \vec{\nabla} \times \vec{\nabla} \times \xi\hat{k}$, if $\nabla^2\Psi = -k_s{}^2\Psi$ and $\nabla^2\xi = -k_s{}^2\xi$. Now the ξ's and Ψ's are expanded in Bessel and cosine functions.

$$k_s{}^2\xi = [D_oH_o{}^{(1)}(k_{sc}r) + 2\sum_{n=1}^{\infty} D_n i^n \frac{d\cos n\theta}{d\theta} H_n{}^{(1)}(k_{sc}r)]e^{i(k_{cs}z-\omega t)} \quad (14)$$

$$ik_{cs}\Psi = [E_oH_o{}^{(1)}(k_{sc}r) + 2\sum_{n=1}^{\infty} E_n i^n \frac{d\cos n\theta}{d\theta} H_n{}^{(1)}(k_{sc})]e^{i(k_{cs}z-\omega t)} \quad (15)$$

$$(k_s')^2\xi' = [D_o'J_o(k_{sc}'r) + 2\sum_{n=1}^{\infty} D_n'i^n \frac{d\cos n\theta}{d\theta} J_n(k_{sc}'r)]e^{i(k_{cs}z-\omega t)} \quad (16)$$

$$ik_{cs}\Psi' = [E_o'J_o(k_{sc}'r) + 2\sum_{n=1}^{\infty} E_n'i^n \frac{d\cos n\theta}{d\theta} J_n(k_{sc}'r)]e^{i(k_{cs}z-\omega t)} \quad (17)$$

When the velocities and temperature are expressed in terms of the potentials by equations (5) and (6), the eight boundary conditions can be expressed in terms of eight sets of undetermined coefficients. Due to the orthogonality of the $\cos n\theta$'s, the boundary conditions must hold for each order of coefficients. This results in eight equations and eight unknowns for each order, n, of coefficients. The resulting equations are

(a) $a_{cc}J_n'(a_{cc}) + B_n a_{cc}H_n{}^{(1)}{}'(a_{cc}) + C_n a_{tc}H_n{}^{(1)}{}'(a_{tc}) - E_n a_{sc}H_n{}^{(1)}{}'(a_{sc}) + n^2D_nH_n{}^{(1)}(a_{sc}) = -i\omega[B_n'a_{cc}'J_n'(a_{cc}') + C_n'a_{tc}'J_n'(a_{tc}') - E_n'a_{sc}'J_n'(a_{sc}') + n^2D_n'J_n(a_{sc}')]$, (18)

(b) $J_n(a_{cc}) + B_nH_n{}^{(1)}(a_{cc}) + C_nH_n{}^{(1)}(a_{tc}) - E_nH_n{}^{(1)}(a_{sc}) + D_n a_{sc}H_n{}^{(1)}{}'(a_{sc}) = -i\omega[B_n'J_n(a_{cc}') + C_n'J_n(a_{tc}') - E_n'J_n(a_{sc}') + D_n'a_{sc}'J_n'(a_{sc}')]$, (19)

(c) $a_{cs}{}^2J_n(a_{cc}) + a_{cs}{}^2B_nH_n{}^{(1)}(a_{cc}) + a_{cs}{}^2C_nH_n{}^{(1)}(a_{tc}) + a_{sc}{}^2E_nH_n{}^{(1)}(a_{cc}) = -i\omega[a_{cs}{}^2B_n'J_n(a_{cc}') + a_{cs}{}^2C_n'J_n(a_{tc}') + a_{sc}'{}^2E_n'J_n(a_{sc}')]$, (20)

(d) $b_c[J_n(a_{cc}) + B_nH_n{}^{(1)}(a_{cc})] + b_tC_nH_n{}^{(1)}(a_{tc}) = -i\omega[b_c'B_n'J_n(a_{cc}') + b_t'C_n'J_n(a_{tc}')]$, (21)

(e) $K[a_{cc}b_c(J_n'(a_{cc}) + B_nH_n{}^{(1)}{}'(a_{cc})) + C_nb_ta_{tc}H_n{}^{(1)}{}'(a_{tc})] = -i\omega K'[B_n'b_c'a_{cc}'J_n'(a_{cc}') + C_n'b_t'a_{tc}'J_n'(a_{tc}')]$, (22)

(f) $n\{[(a_s{}^2-2a_c{}^2)J_n(a_{cc}) - 2a_{cc}{}^2J_n''(a_{cc})] + B_n[(a_s{}^2 - 2a_c{}^2)H_n(a_{cc}) - 2a_{cc}{}^2H_n{}^{(1)}{}''(a_{cc})] + C_n[(a_s{}^2-2a_t{}^2)H_n{}^{(1)}(a_{tc}) - 2a_{tc}{}^2H_n{}^{(1)}{}''(a_{tc})] + 2E_na_{sc}{}^2H_n{}^{(1)}{}''(a_{sc}) + 2D_nn^2[H_n{}^{(1)}(a_{sc}) - a_{sc}H_n{}^{(1)}{}'(a_{sc})]\} =$ (23)

$$B_n'[(\omega^2\rho'R'^2 - 2\mu'a_c'^2)J_n(a_{cc}') - 2\mu'a_{cc}'^2J_n''(a_{cc}')] +$$

$$C_n[(\omega^2\rho'R'^2 - 2\mu'a_t'^2)J_n(a_{tc}') - 2\mu'a_{tc}'^2J_n''(a_{tc}')] +$$

$$2\mu'E_n'a_{sc}'^2J_n(a_{sc}') + 2\mu'D_n'n^2[J_n(a_{sc}') - a_{sc}'J_n(a_{sc}')], \tag{23}$$

(g) $$n\{a_{cc}J_n'(a_{cc}) - J_n(a_{cc}) + B_n[a_{cc}H_n^{(1)}'(a_{cc}) - H_n^{(1)}(a_{cc})] +$$

$$C_n\,[a_{tc}H_n^{(1)}(a_{tc}) - H_n^{(1)}(a_{tc})] + \frac{D_n}{2}\,[n^2H_n^{(1)}(a_{sc}) - a_{sc}H_n^{(1)}'(a_{sc}) +$$

$$a_{sc}^2H_n^{(1)}''(a_{sc})] + E_n\,[H_n^{(1)}(a_{sc}) - a_{sc}H_n^{(1)}'(a_{sc})]\} =$$

$$\mu'\{B_n'[a_{cc}'J_n'(a_{cc}') - J_n(a_{cc}')] + C_n'[a_{tc}'J_n'(a_{tc}') - J_n(a_{tc}')] +$$

$$\frac{D_n'}{2}\,[n^2J_n(a_{sc}') - a_{sc}'J_n'(a_{sc}') + a_{sc}'^2\,J_n''(a_{sc}')] + E_n'[J_n(a_{sc}') -$$

$$a_{sc}'J_n'(a_{sc}')]\}, \text{ and} \tag{24}$$

(h) $$2\eta a_{cc}a_{cs}[J_n'(a_{cc}) + B_nH_n^{(1)}'(a_{cc})] + 2\eta a_{tc}a_{cs}C_nH_n^{(1)}'(a_{tc}) +$$

$$\eta E_nH_n'(a_{sc})[a_{sc}^2 - a_{cs}^2]a_{sc}/a_{cs} + \eta D_nn^2a_{cs}H_n^{(1)}(a_{sc}) = 2\mu'a_{cc}'a_{cs}$$

$$B_n'J_n'(a_{cc}') + 2\mu'a_{tc}'C_n'J_n'(a_{tc}')a_{cs} + \mu'D_n'n^2a_{cs}J_n(a_{sc}') +$$

$$\mu'E_n'J_n'(a_{sc}')a_{sc}'[a_{sc}'^2 - a_{cs}^2]/a_{cs}. \tag{25}$$

These eight simultaneous equations are solved numerically for the n = 0, 1, and 2. When k_cR' and $k_c'R'$ are less than one, the series converges rapidly, and the first three terms provide an excellent approximation to the solution.

A rather lengthy calculation, modeled after the Epstein and Carhart (6) spherical development, expresses the attenuation coefficient, α, for fibers at an angle ε to the radiation as

$$\alpha = \frac{-4fr}{\pi R'^2k_c}\,[\text{Real}(B_o) + \sum_{n=1}^{\infty} 2\text{Real}(B_n)]. \tag{26}$$

The B_n's are a function of ε; therefore, to find α for a random orientation the simultaneous equations must be evaluated at a series of ε's between 0° and 90° and averaged. This is done by numerically integrating the following:

$$\alpha_{\text{random}} \simeq \frac{-4fr}{\pi R'^2k_c} \int_0^{\pi/2} \text{Real}[B_o + 2(B_1 + B_2)]\cos\varepsilon\, d\varepsilon. \tag{27}$$

This process can be repeated at different frequencies, and the attenuation vs. frequency can be predicted from the physical properties of the slurry.

TABLE I

SYNTHETIC FIBER PROPERTIES

Fiber Type	Radius, μm	Rod Velocity[a] 60 KHz, mm/μsec	Instron Modulus, 10^9 Nt/m^2	Figures	Comments
Nylon 6,6	13-16	1.66 (wet)	3.09	5	
Nylon 6	110-120	2.13 (dry)	2.87	6	
Polyester	13	4.00 (wet)	10.7	7, 8	
Rayon	11-15	0.91 (wet)		9, 10	Regular modulus
Rayon	7-10	1.27 (wet)		11	Hi-wet modulus

[a]Rod velocity $\simeq (E'/\rho')^{1/2}$.

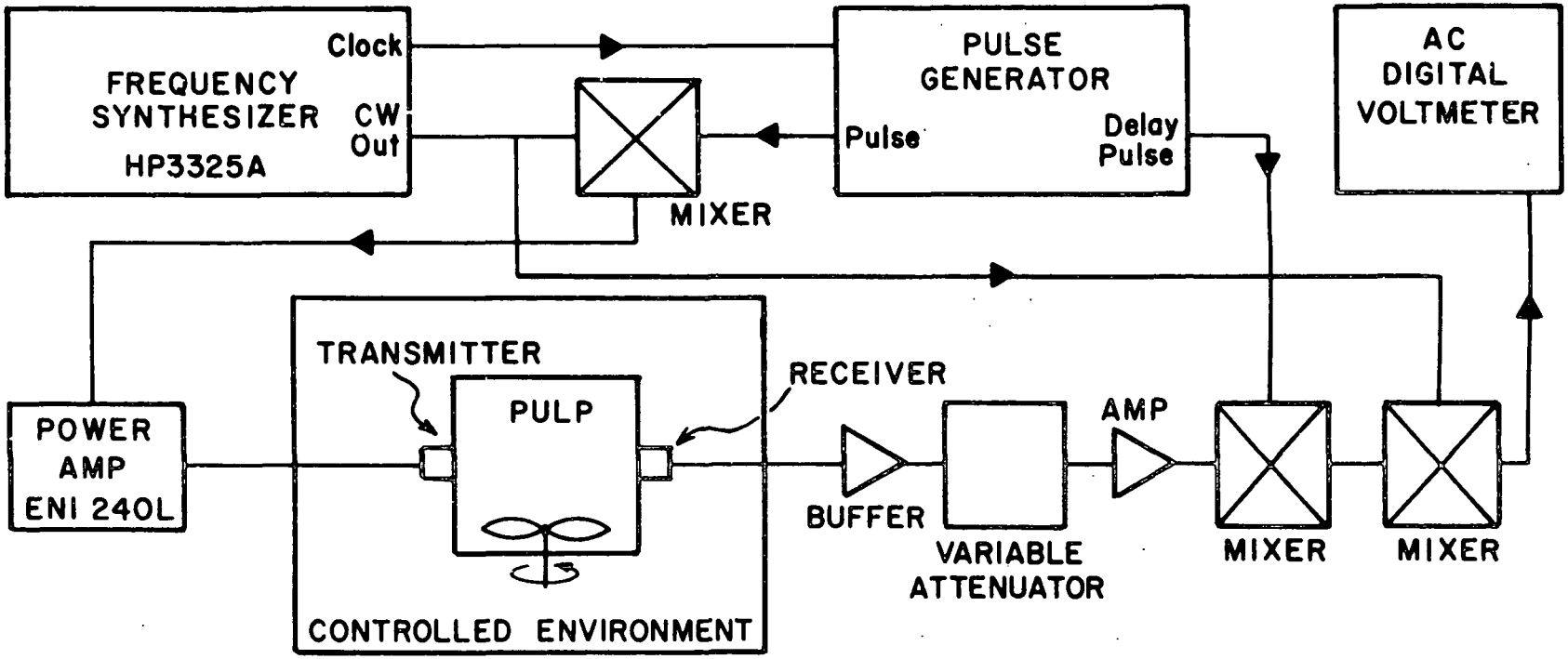

Figure 1. Schematic diagram of the apparatus for the ultrasonic characterization of fiber suspensions.

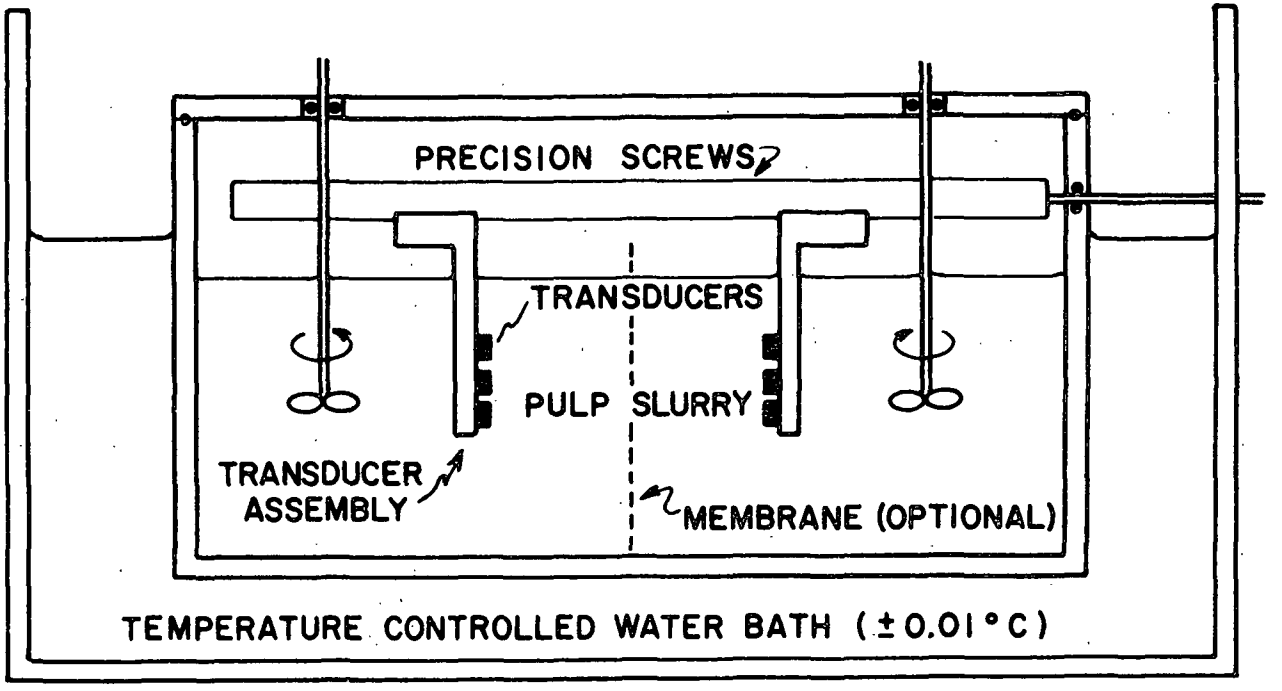

Figure 2. Simplified cross section of sample chamber.

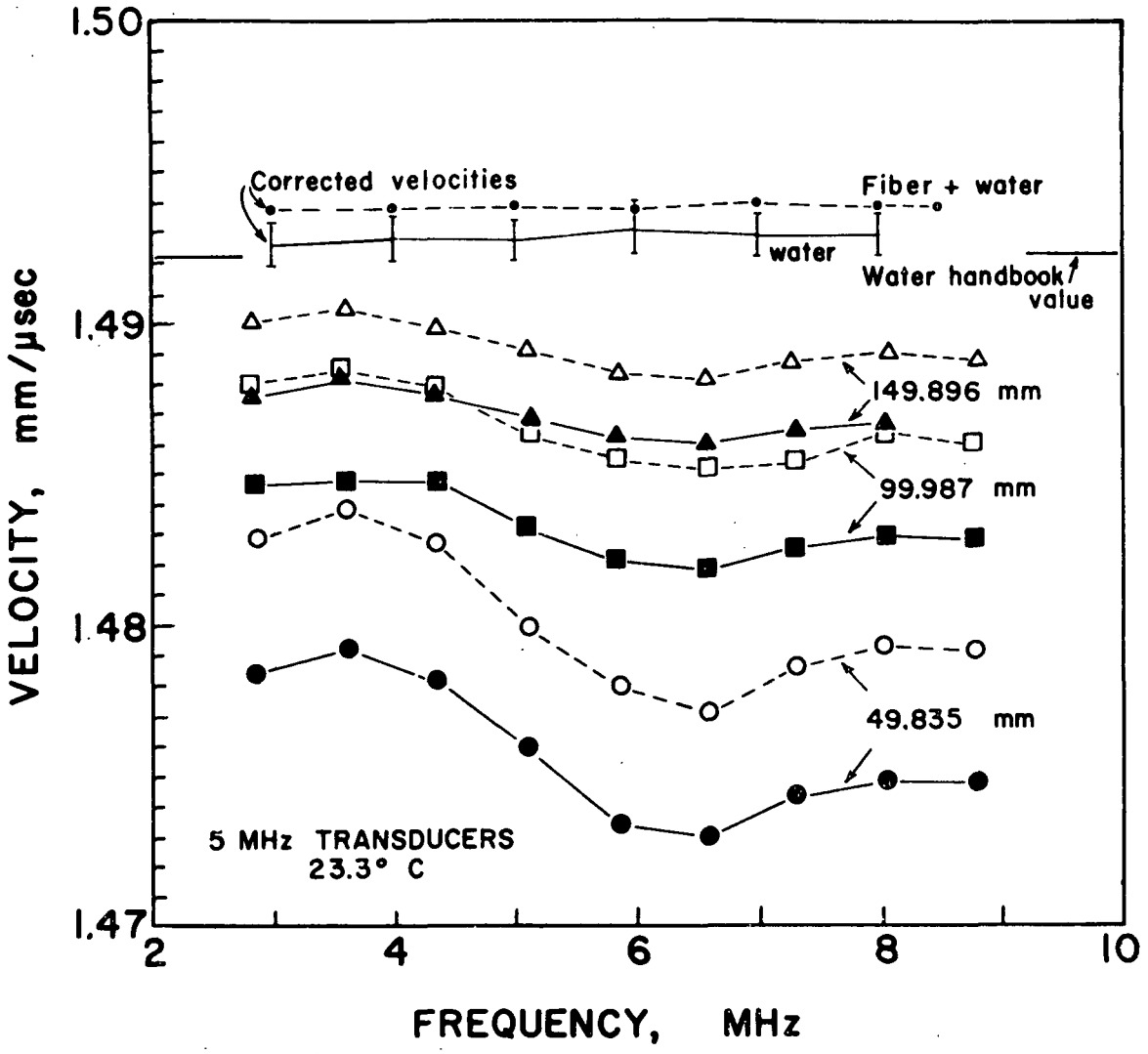

Figure 3. Apparent and corrected velocities as a function of frequency. The solid points and curves are distilled water at transducer separations of 49.835 mm (●), 99.987 mm (■), and 149.896 mm (▲). The open points and dashed lines are for a 0.48% consistency bleached kraft pulp, at the same transducer separations. The two uppermost curves are the corrected water and slurry velocities.

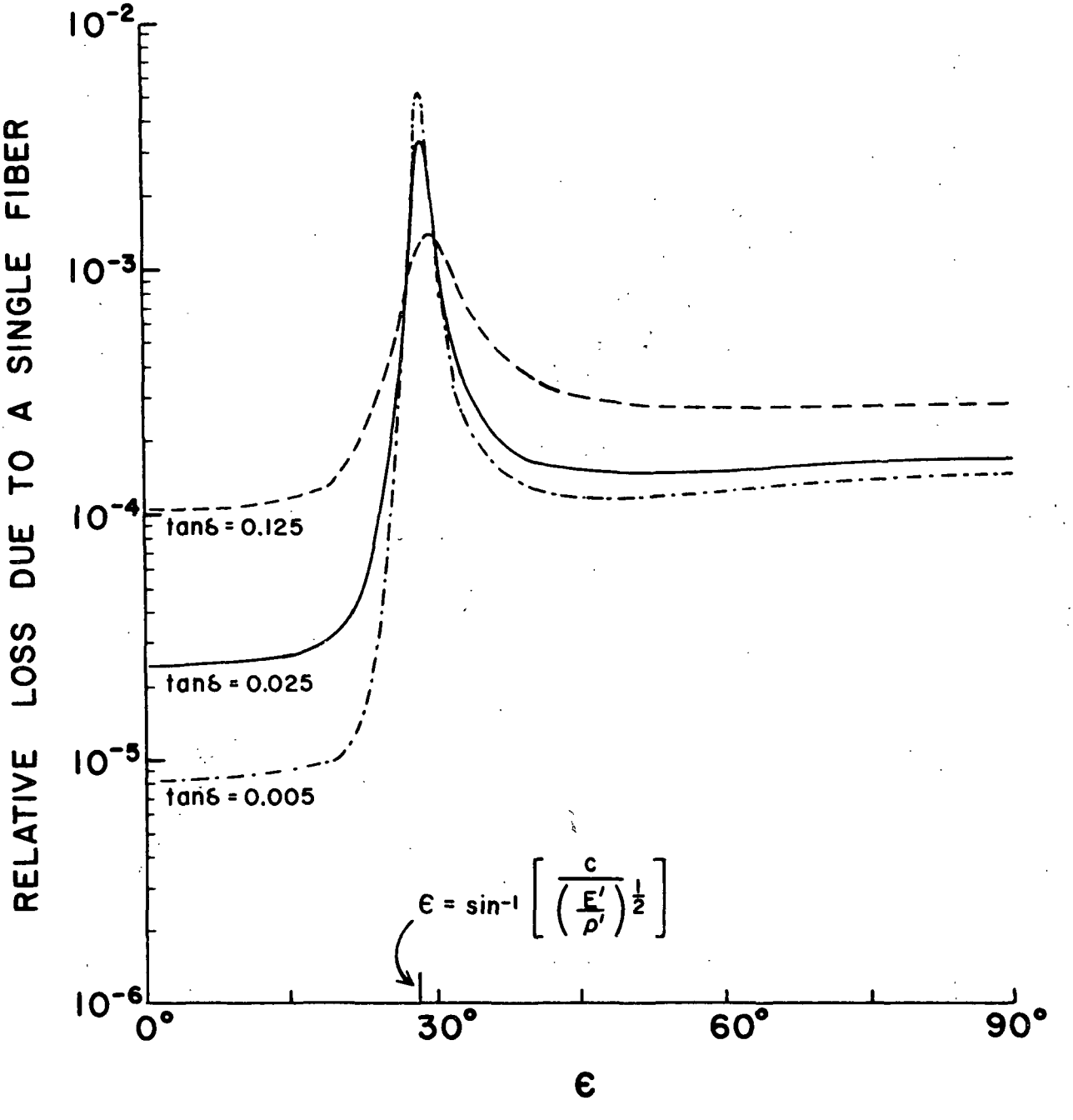

Figure 4. Theoretical plots of the relative loss per single fiber vs. the angle, ϵ, between the incoming radiation and the plane of the fiber. The slurry parameters are ρ = 996 kg/m^3; ρ' = 1340 kg/m^3; η = 9.4 x 10^{-4} nt·sec/m^2; K = 0.59 watts/m°K; K' = 0.038 watts/m°K; c = 1490 m/sec; c' = 4000 m/sec; ν' = 0.35; Cp = 4.14 x 10^3 J/kg°K; Cp' = 1.02 x 10^3 J/kg°K; β = 2.36 x 10^{-4}/°K; β' = 1.7 x 10^{-5}/°K; f = 1 MHz; T = 296°K; and R' = 13 x 10^{-6} m. A list of symbols is in the appendix.

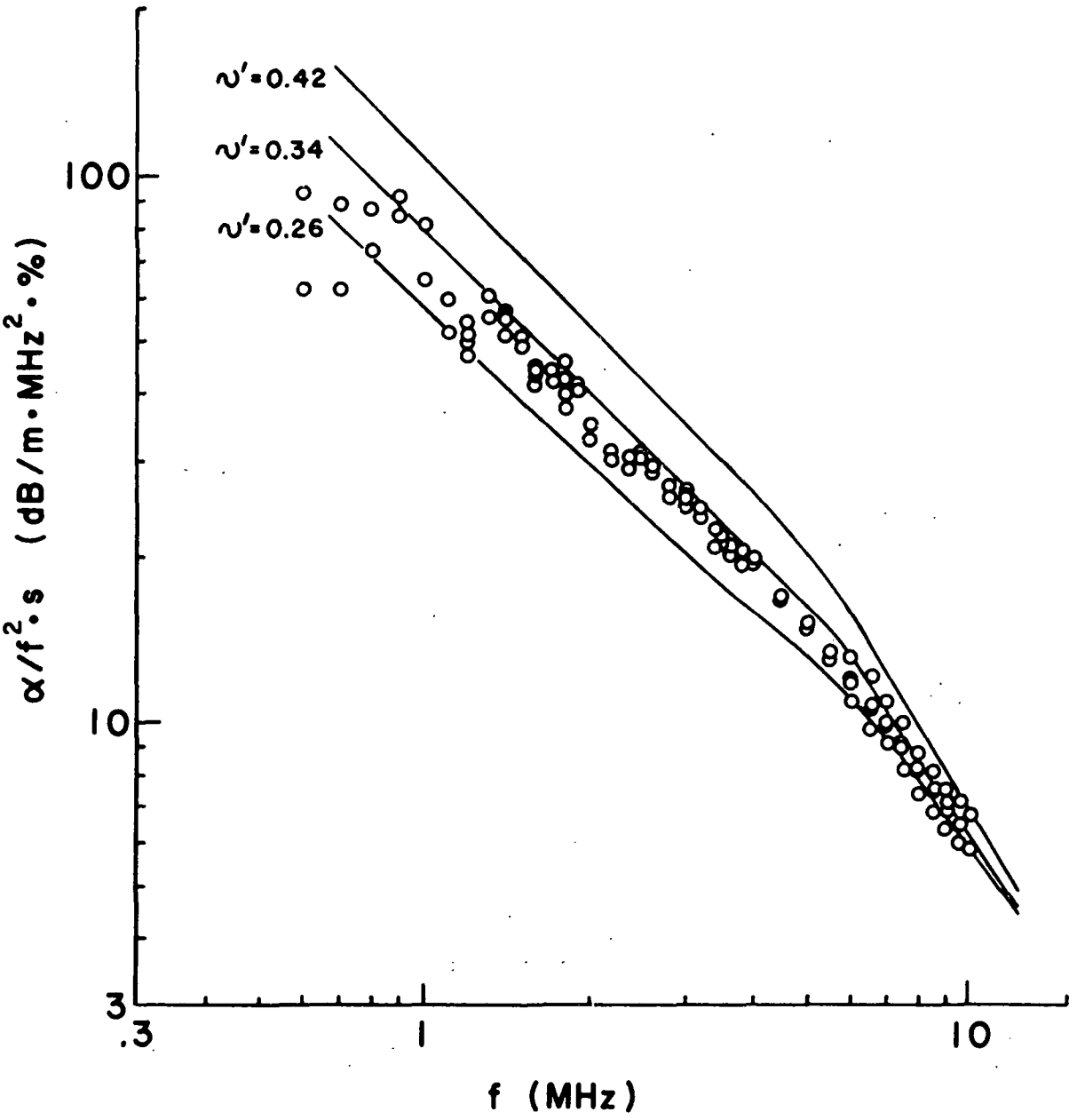

Figure 5. Experimental attenuation data for a nylon 6,6 fiber slurry with radii from 13 to 16 μm and a length of 2.3 mm. The accompanying lines are theoretical curves for different values of fiber Poisson's Ratio. Model fiber parameters are $\rho' = 1090$ kg/m^3; $V_R' = 1660$ m/sec; $K' = 0.36$ watts/m°K; $Cp' = 1.42 \times 10^3$ J/kg°K; $\beta' = 1.0 \times 10^{-5}$/°K; $\tan\delta = 0.1$; $R' = 15.2 \times 10^{-6}$ m; and $s = 1.08\%$. For water parameters see Figure 4.

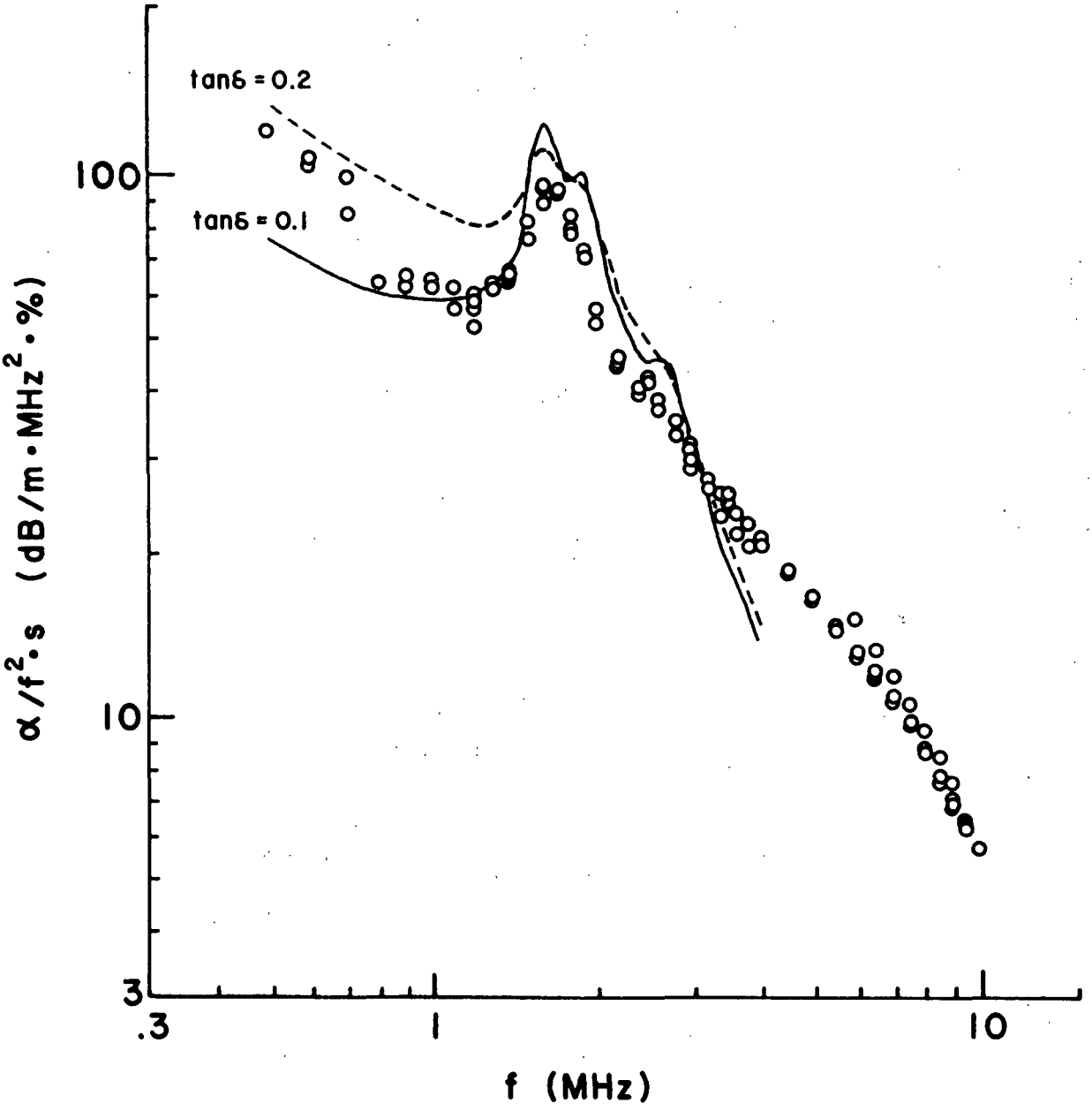

Figure 6. Experimental attenuation data for a nylon 6 fiber slurry with radii from 110 to 120 μm and a length of 2.3 mm. The theoretical lines are for different values of the loss tangent. Model fiber parameters are $\rho' = 1090$ kg/m^3; $c' = 1340$ m/sec; $\nu' = 0.30$; $K' = 0.36$ watts/m°K; $Cp' = 1.42 \times 10^3$ J/kg°K; $\beta' = 1.0 \times 10^{-5}$/°K; $R' = 115 \times 10^{-6}$ m; and $s = 1.08\%$. Figure 4 has the water parameters.

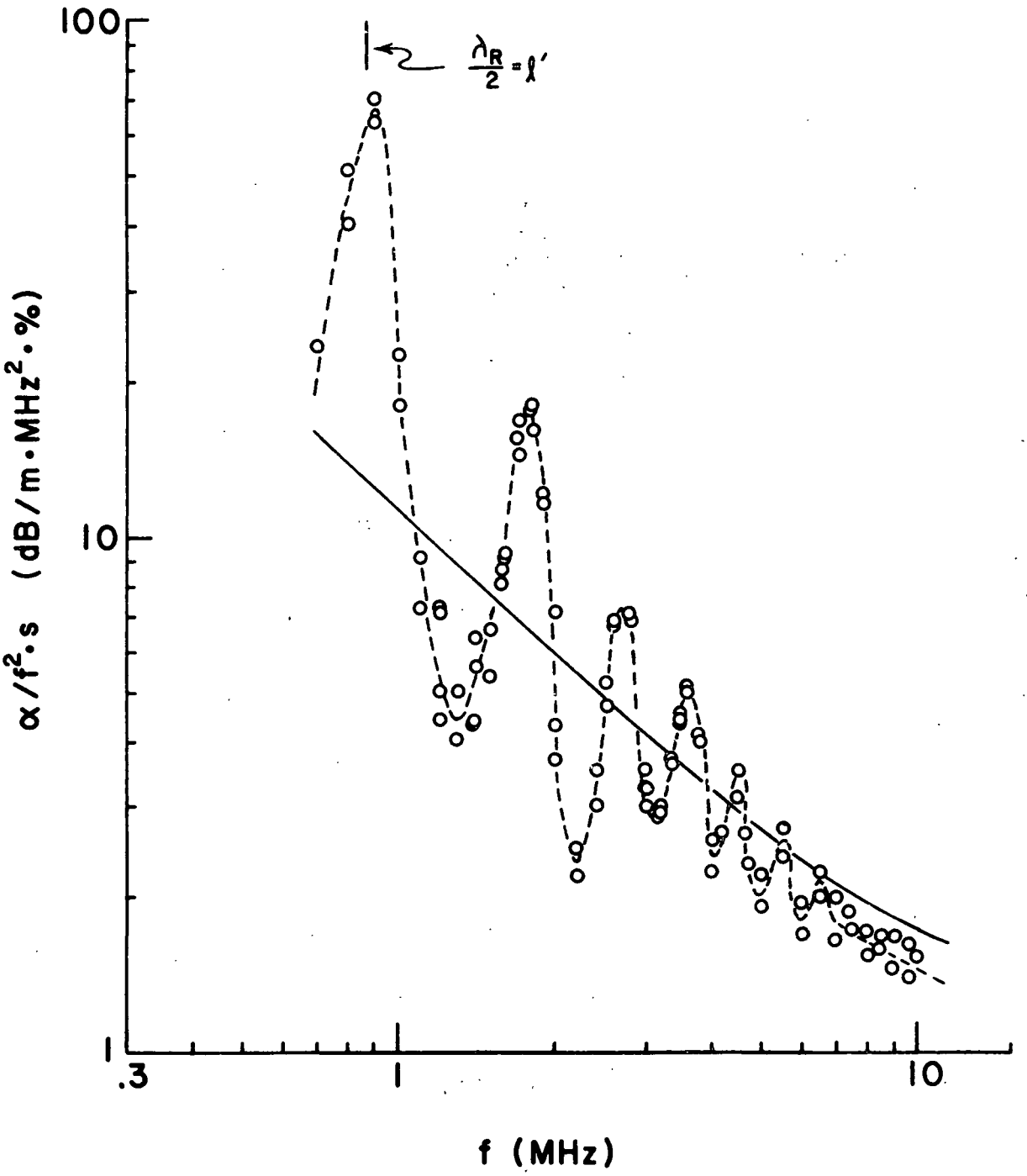

Figure 7. Experimental attenuation data for a polyester fiber slurry with a radius of 10.7 μm and a length of 2.30 mm. The model fiber parameters for the theoretical curve are $\rho' = 1340$ kg/m^3; $c' = 5860$ m/sec; $\nu' = 0.4$; $K' = 3.8 \times 10^{-2}$ watts/m°K; $Cp' = 1.02 \times 10^3$ J/kg°K; $\beta' = 1.7 \times 10^{-5}$/°K; $R' = 13 \times 10^{-6}$ m; and $s = 1.00\%$.

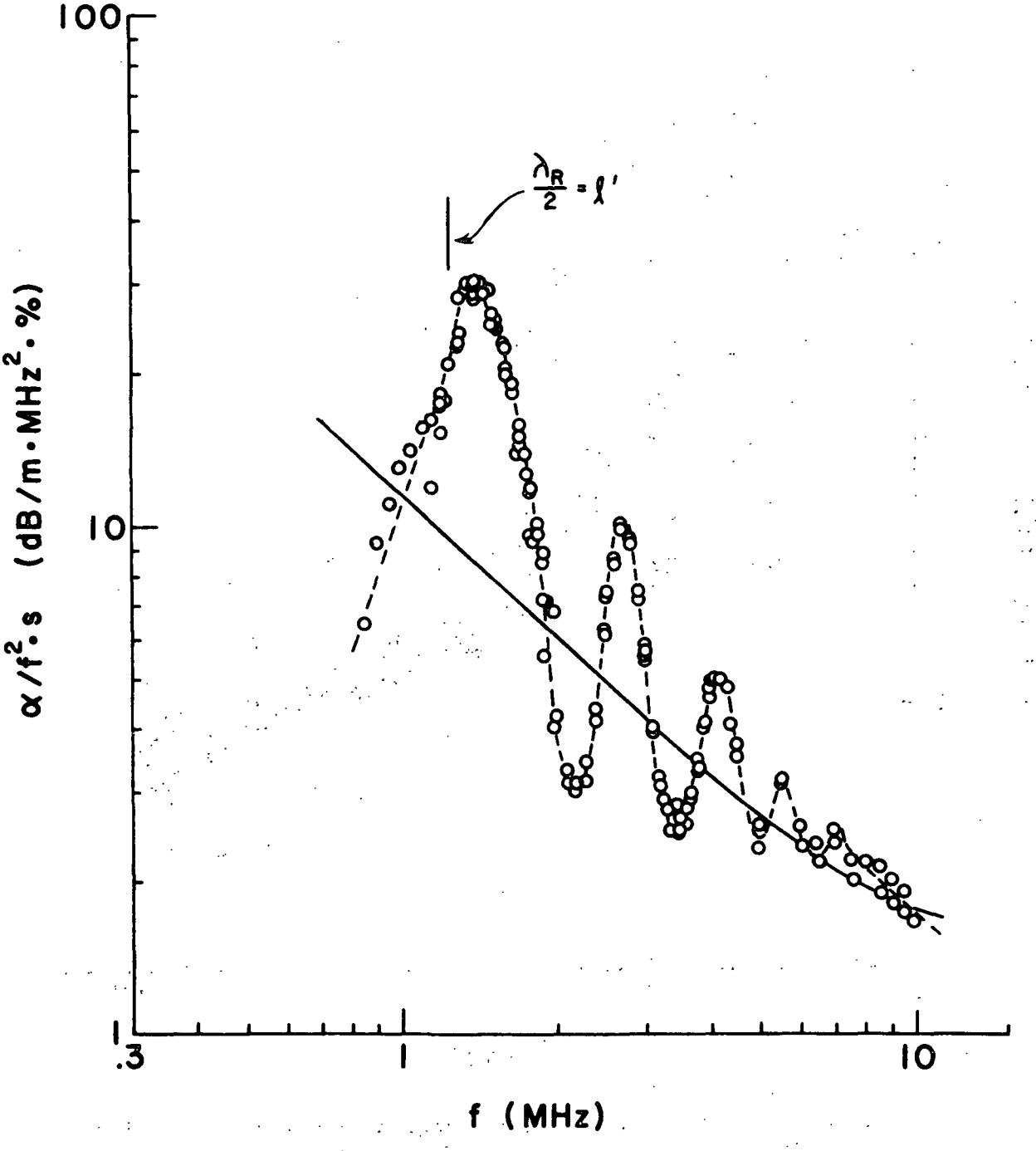

Figure 8. Experimental attenuation data for a polyester fiber slurry identical to that of Figure 7, except $\ell' = 1.66$ mm. The model curve is the same as in Figure 7.

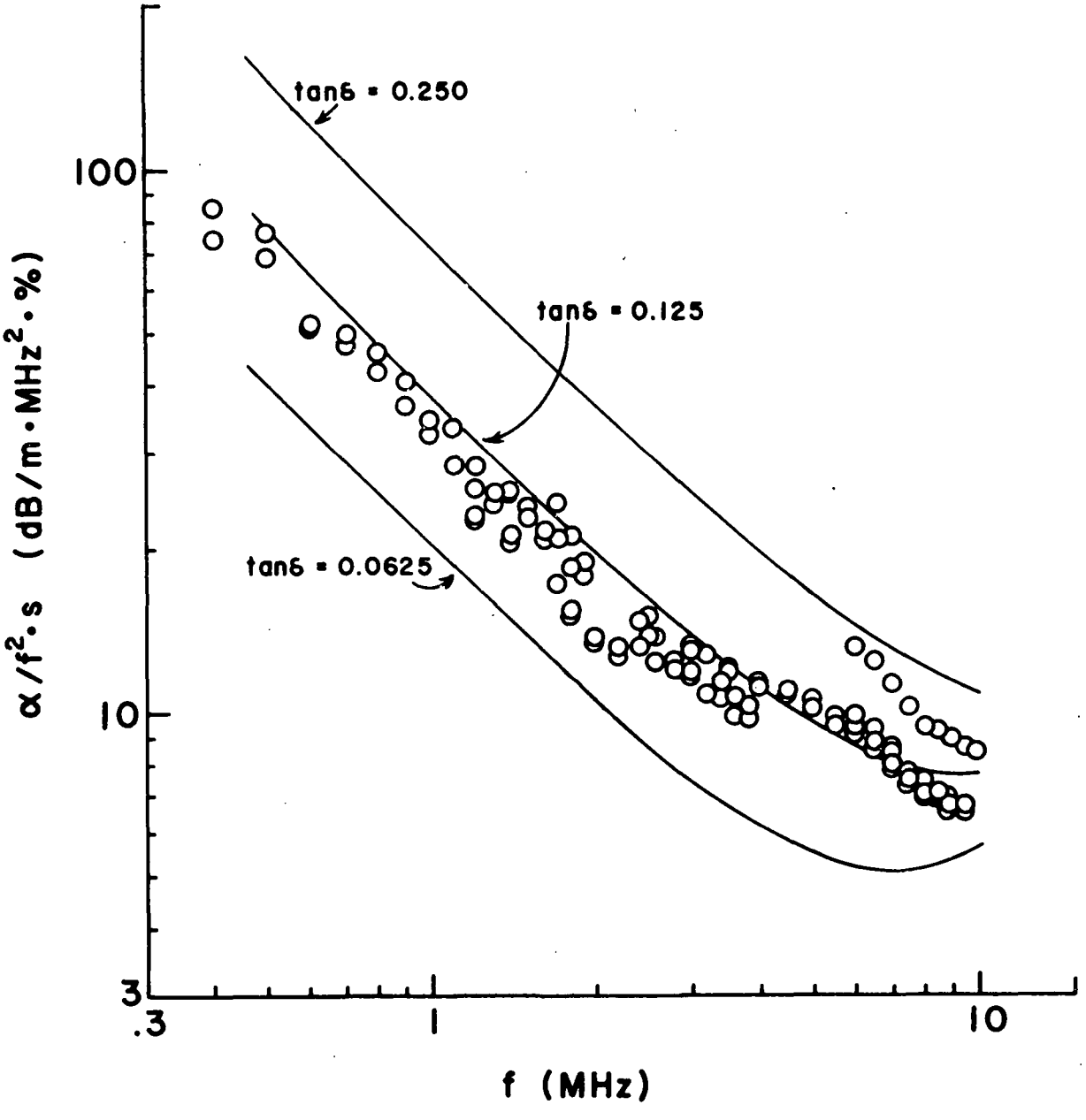

Figure 9. Experimental attenuation data for regular modulus, 2.3-mm-long rayon fibers with radii from 11-15 μm. The theoretical curves have different loss tangents. The model fiber parameters are $\rho' = 1400$ kg/m^3; $c' = 1090$ m/sec; $\nu' = 0.32$; $K' = 0.15$/m°K; $Cp' = 1.5 \times 10^3$ J/kg°K; $\beta' = 3.6 \times 10^{-4}$/°K; $R' = 13 \times 10^{-6}$ m; and $s = 1.25\%$.

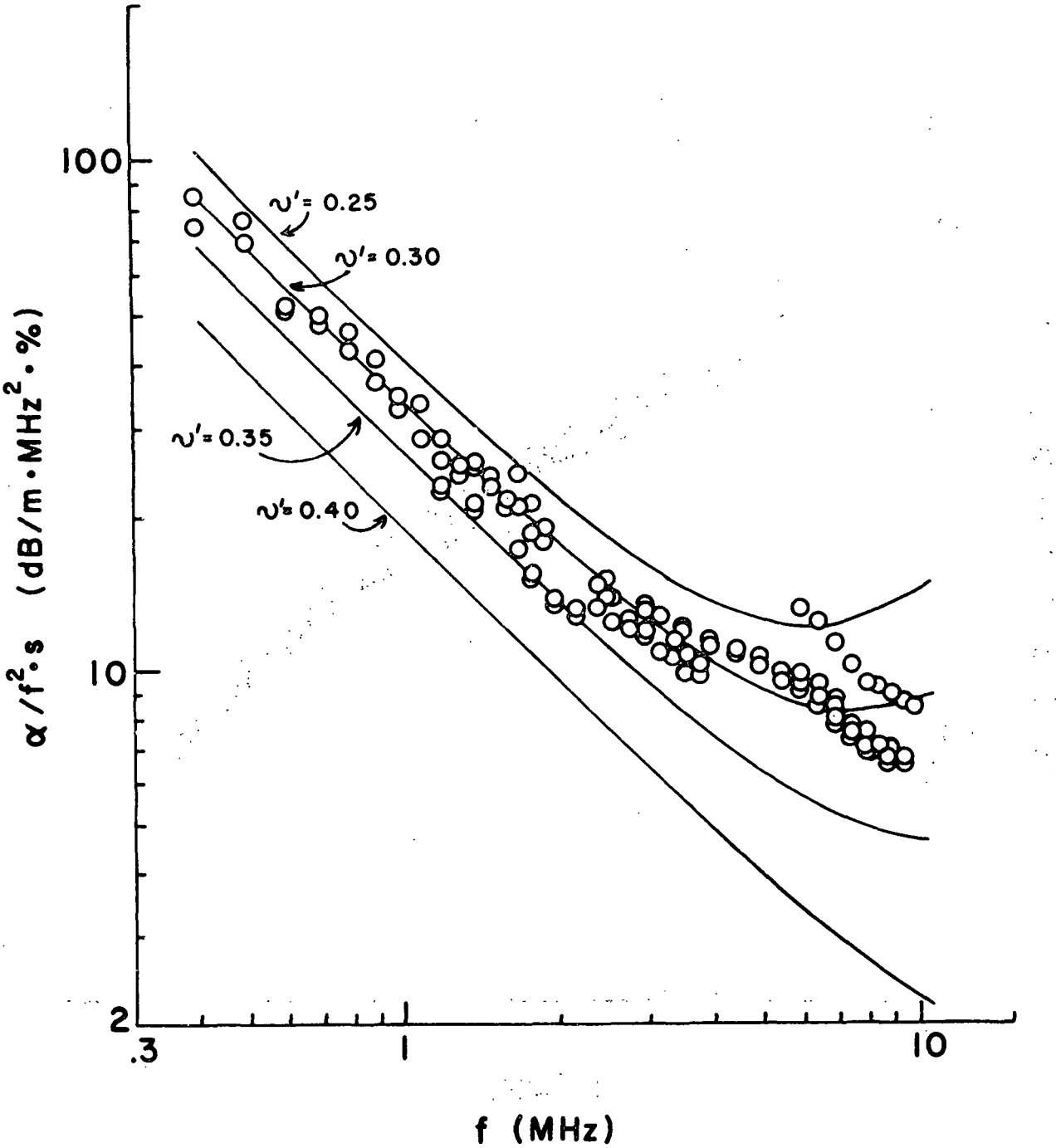

Figure 10. Experimental attenuation data for regular modulus, 2.3 mm long rayon fibers with radii from 11-15 μm. The theoretical curves have different Poisson's ratios. The model fiber parameters are $\rho' = 1400$ kg/m^3; $c' = 1090$ m/sec; $K' = 0.15$/m°K; $Cp' = 1.5 \times 10^3$ J/kg°K; $\beta' = 3.6 \times 10^{-4}$/°K; $R' = 13 \times 10^{-6}$ m; $\tan\delta = 0.1$; and $s = 1.25\%$.

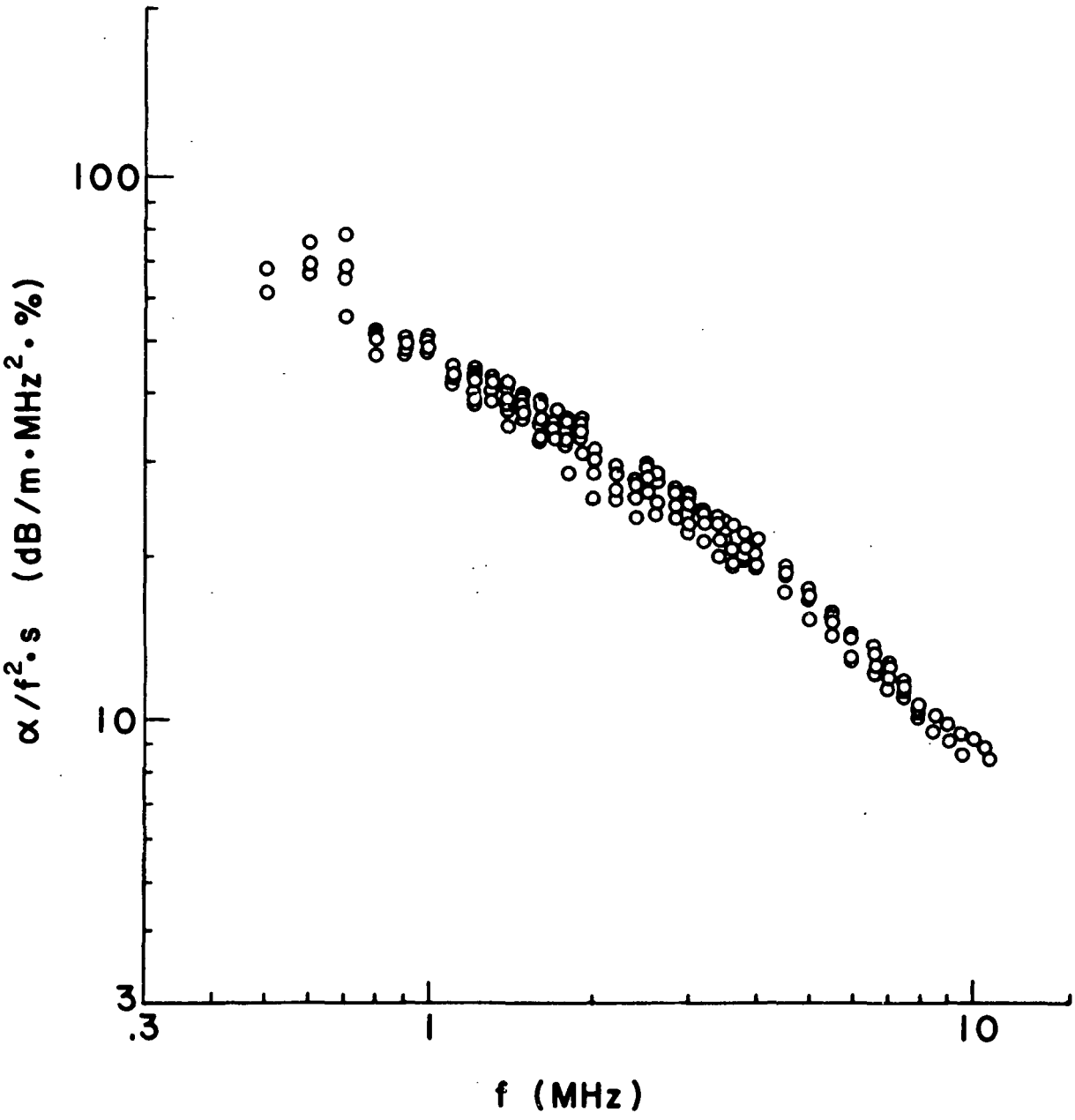

Figure 11. Experimental attenuation data for high wet modulus, 2.3 mm long rayon fibers with radii from 7 to 10 μm.

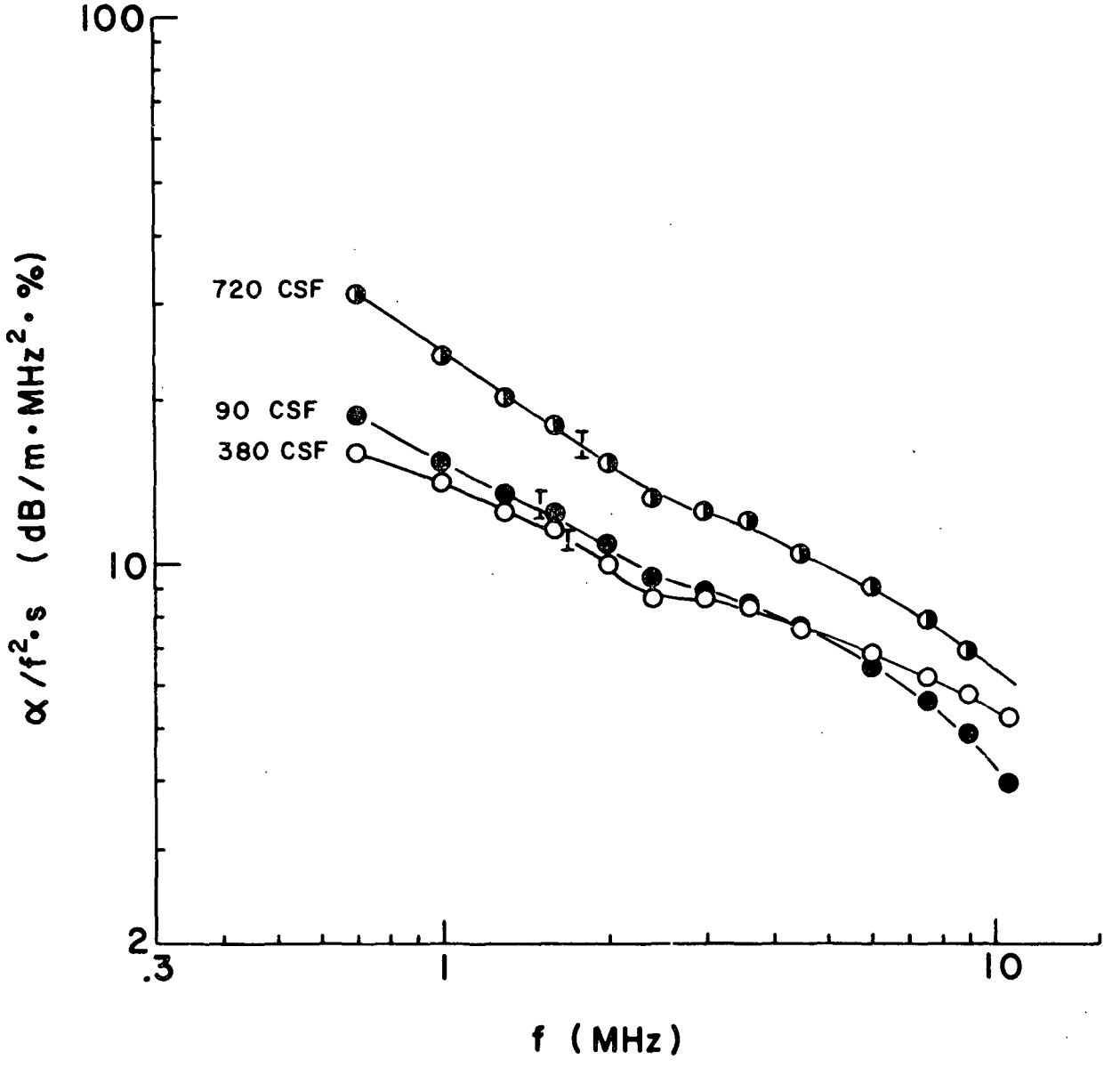

Figure 12. Average experimental attenuation data for a bleached kraft softwood pulp at freenesses of 720, 380, and 90 CSF. Each data point is the average of about 25 measurements.